RSC Advances

PAPER

View Article Online
View Journal | View Issue

Check for updates

Cite this: *RSC Adv.*, 2020, **10**, 35287

Low density magnetic silicate-nickel alloy composite hollow structures: seed induced direct assembly fabrication and catalytic properties†

Gaiping Du,[ab] Bin Liao,[a] Ran Liu,[ab] Zhenguo An *[a] and Jingjie Zhang *[a]

Received 30th January 2020
Accepted 16th September 2020

DOI: 10.1039/d0ra00893a

rsc.li/rsc-advances

An efficient seed induced direct assembly route is designed for the controlled synthesis of hollow microsphere supported catalysts (HMSCs) with nickel alloy as the active material. The inherent magnetic response of nickel alloy endows HMSCs magnetic separability, and the hollow interior of the support opens a new avenue for self-floating separation. It is found that the introduction of P and Co contributes largely to the improvement of the catalytic performance of the products, which may attributed to synergistic effects and electron transfer. Moreover, the loading amounts of alloy nanoparticles can be easily tailored through properly monitoring the reaction conditions. With the optimized loading of 2.68 wt%, the k_N of HMSC–NiCoP-2.68 wt% reaches 14.0 s^{-1} g^{-1} for the catalytic reduction of *p*-nitrophenol (4-NP), which is higher than commercial 5 wt% Pd/C of 11.6 s^{-1} g^{-1} under the same conditions. This work provides additional insights into preparation and property control of an easily separable supported non-noble metal catalyst, which holds potential to be extended to the preparation and property control of other metal nanocatalysts on various supports.

1. Introduction

Over the past decades, the research of nanocatalysts has been in full swing. Due to its surface defects and coordination unsaturation, the active site density of nanoparticles (NPs) is higher than their bulk counterparts, resulting in distinguished catalytic performance.[1] However, the aggregation and difficult separation of NPs during synthesis and application are supposed to negatively effect the performance and recyclability of nano-scale catalysts.[2–4] The synthesis of well dispersed and easily collectable small size catalysts is challenging. In this regard, researchers propose supported core–shell structures. Xin Zhang *et al.* coated mesoporous SiO_2 on ultrathin Ni_3FeN with the size of ≈20 nm to protect the ultrathin sheets from coalescence.[5] Chun-Chao Hou *et al.* dispersed Co-doped nickel phosphide NPs on graphene oxide (GO) to prevent magnetic NPs aggregation.[6] Nevertheless, there is still serious irreversible agglomeration over the active particles with the loading amounts increasing or in the catalytic process, resulting in increasing particle size and weakened catalytic activity. There are also reports about loading NPs in the cavity of hollow structures for better dispersion of NPs.[7] However, this structure may hinder the mass transfer process in the solution, and also the aggregation cannot be avoided when the loading amounts continue to increase. Till now, the development of supported nanocatalysts that can simultaneously achieve controllable loading amount, good dispersion of the loaded content, easy separation and recycling, and well accessibility of the active sites remains a big challenge. Therefore, for the sake of both academic study and application, supported nanocatalysts with properly selected supports and well controlled loading of the active sites need to be developed in more details.

Recently, more attention is paid to the catalysis of ferromagnetic transition metal nanoparticles (FTM NPs) and supported-FTM NPs.[8,9] Due to their special electron structures and large surface area to volume ratio with abundance of surface defects, FTM NPs exhibit efficient catalytic activity, especially ultrasmall FTM NPs.[10–13] Besides, FTMs are abundant in reserves, low in price, and can be used as a new type of catalyst to replace expensive precious metal catalysts.[6,9] FTM NPs is also an excellent separation material, which can be separated and enriched by the external magnetic field due to its native ferromagnetic properties. However, similar to other nanocatalysts, nano-scale FTMNPs also possess strong tendency to aggregate. More seriously, the inherent ferromagnetism of FTM NPs brings additional magnetic dipole interaction that

---

[a] *Key Laboratory of Photochemical Conversion and Optoelectronic Materials, Technical Institute of Physics and Chemistry, Chinese Academy of Sciences, Beijing 100190, P. R. China. E-mail: zgan@mail.ipc.ac.cn; jjzhang@mail.ipc.ac.cn; Fax: +86 10 82543690; Tel: +86 10 82543690*

[b] *University of Chinese Academy of Sciences, Beijing 100049, P. R. China*

† Electronic supplementary information (ESI) available: SEM and optical microscopy images of HGMs, AHGMs, HMSC–NiCoP, HMSC–Ni and pure NiCoP. XPS peak parameters of HMSC–Ni, HMSC–NiP and HMSC–NiCoP. The kinetic parameter of HMSC–Ni, HMSC–NiP and HMSC–NiCoP. The SEM images of depositing other metallic alloy on different supported spheres including HGMs and hollow phenolic resin microspheres (HPRMs). See DOI: 10.1039/d0ra00893a

favors the aggregation.[10] According to the previous reports, the deposition of FTM NPs or noble metal NPs onto various supports, such as graphene,[14–17] oxides,[18–20] and mesoporous silica,[21,22] or composite substrate[23,24] have been extensively explored to achieve better dispersion, easier separation, and cooperatively enhanced performances. However, the main problem lies in the tedious and costly synthetic route (including high temperature phosphating, complicated multi-step, and time-consuming reaction process), and the inherent shortcoming of the support that hinders effective separation and reuse of the catalyst.

Herein, we proposed a versatile high-efficient and low temperature route involving seed-induced reduction and *in situ* assembly for the controlled loading of nickel-based nanocatalysts. Interestingly, during the reduction and *in situ* assembly process, the chemical composition can be conveniently tailored by rational design of the reaction composition. With hollow glass microspheres (HGMs) as a low density support, supported catalysts with nickel–cobalt–phosphorous as active material (HMSC–NiCoP) have been successively prepared with controllable loading amounts. For the catalytic activity investigation, *p*-nitrophenol (4-NP), a contaminant in wastewater whose reduzate (*p*-aminophenol, 4-AP) is a valuable intermediate in chemical industry,[8,25,26] is employed as a model for catalytic hydrogenation. The component and loading amount dependence of the catalytic activity of our HMSC are systematically studied. Moreover, the catalytic activity for the hydrogenation of some other dyes, such as methylene blue (MB), rhodamine B (RhB), methyl orange (MO), and Alizarin red S (ArS) of our HMSC–NiCoP catalysts were also studied. On the other hand, our loading strategy is also proved to be available for the controlled loading of other metallic nanocatalysts. So it is safe to say that our synthetic strategy holds potential to be extended to the preparation and property control of other metal nanocatalysts on various supports.

2. Experimental section

All reagents were of analytical grade and used as received without further purification.

2.1 Preparation of AHGMs

The HGMs used in this work are manufactured through soft chemical method by our laboratory[27,28] and its physical parameters are summarized in Table S1.† The activated hollow glass microspheres (AHGMs) are prepared by a stepwise active process in aqueous solution, where the HGMs were modified with active sites. Firstly, the 15 g HGMs were added into 200 mL ethanol water solution (volume ratio is 1 : 1) containing 10 g KH550 (3-aminopropyltriethoxysilane) to obtain surface aminated HGMs. The suspension was stirred for 30 min and filtered. Then the powders were dried in a constant temperature drying chamber at 60 °C overnight. Secondly, the collected particles were dispersed into 150 mL distilled water mixed with 5.00 g $SnCl_2$ and 15 mL concentrated HCl (38 wt%), with magnetic stirring at 50 °C for 10 min and filtered. Thirdly, the collected wet powders were redispersed into 150 mL aqueous solution containing 0.20 g $PdCl_2$ and 5 mL concentrated HCl (38 wt%), then stirred at 50 °C for 10 min. Finally, the particles obtained above were reduced in 150 mL aqueous solution containing 0.28 mol L^{-1} NaH_2PO_2 solution stirred at 50 °C for 10 min. After filtration and subsequent drying at 60 °C,the AHGMs were obtained.

2.2 Surface assembly of nickel-based alloy

For the preparation of HMSC–NiCoP, a mixed solution was formulated which consisted of 10 g L^{-1} $NiSO_4\cdot6(H_2O)$, 10 g L^{-1} $CoSO_4\cdot7(H_2O)$, 60 g L^{-1} NaH_2PO_2, 60 g L^{-1} $KNaC_4H_{12}O_{10}\cdot6(H_2O)$, 40 g L^{-1} $(NH_4)_2SO_4$. The pH value was adjusted to 9–10 using concentrated ammonia. And then the reaction was taken in a water bath at 70 °C after AHGMs were added. Loading amounts of NiCoP in HMSC–NiCoP is tuned by varying the mass ratio of mixed solution to AHGMs. For the sample obtained with a mass ratio (between the reaction solution and the AHGMs) of 10 : 1, a code name "HMSC–NiCoP-2.68 wt%" was used, which means the loading amounts of NiCoP is 2.68 wt%. In a typical experiment, 50 g mixed solution and 5 g HGMs was applied. For HMSC–NiP, the synthesis process is similar to that of HMSC–NiCoP-2.68 wt% except for the absence of $CoSO_4\cdot7(H_2O)$ in the reaction solution. For HMSC–Ni, the synthesis process is similar to that of HMSC–NiP, while NaH_2PO_2 was substituted by 0.1g L^{-1} hydrazine hydrate (80%).

2.3 Catalytic experiment

In order to investigate the activity of all catalysts, the catalytic experiment was taken using the reductive conversion of 4-NP as a probe reaction. In a typical experiment, 5 mL 5 mmol L^{-1} 4-NP aqueous solution was mixed with 90 mL distilled water in a 200 mL beaker, and then 5 mL 0.5 mol L^{-1} $NaBH_4$ aqueous solution was poured into the beaker. After that 0.10 g sample was added under magnetic stirring at a constant speed and start timing. 5 mL of the mixed solution was taken out every 30 seconds, and the HMSC particles were separated quickly by a magnet. The subnatant was collected and immediately recorded by UV-vis absorption spectra at room temperature. In an analogous procedure, the 4-NP was replaced by methylene blue (MB), rhodamine B (RhB), methyl orange (MO), and Alizarin red S (ArS) respectively to investigated the multiple catalytic property of HMSC–NiCoP-2.68 wt%.

2.4 Cyclic experiment

In the cyclic test, the process is similar to the catalytic experiment except stopping reaction at 120 s. Then the catalysts were separated straightway by floatation and external magnetic field, and washed three times with distilled water for the next cycle.

3. Characterization

The morphologies and sizes of different samples were examined with a field-emission scanning electron microscope (FE-SEM, Hitachi-S4800, Japan) and AxioImager A2m optical microscope. High-resolution transmission electron microscopy

(HRTEM) and selected area electron diffraction (SAED) observations were carried out on a JEM-2100 transmission electron microscope operated under an acceleration voltage of 200 kV. The energy dispersive spectrometer X-ray (EDX) spectrum was obtained with Energy dispersive spectrometer Horiba. Powder X-ray diffraction (XRD) patterns of the samples were recorded on X-ray powder diffraction (*D*/max 2200 PC, Rigaku, Japan) with a Cu Kα ($\lambda = 0.15406$ nm) radiation with a 2θ range from 10°to 80°and a scanning rate of 10 min^{-1}. The recorded patterns were analyzed using JADE 6.0 software to determine peak positions. X-ray photoelectron spectroscopy (XPS) was carried out by a Kratos Axis Ultra (Kratos Analytical, Ltd) equipped with a monochromatized Al Kα X-ray source ($h\nu = 1486.7$ eV) operating at a power of 225 W (15 kV, 15 mA). The carbonaceous C 1s line (284.4 eV) was used as an internal standard to calibrate the binding energies. The spectra were analyzed using XPSPEAK software. The catalytic activity measurement of the catalysts for 4-NP conversion was using UV-visible spectrophotometer (Agilent, Cary 5000) with the wavelength at 400 nm. The X-ray fluorescence spectroscopy (XRF) results were calculated by ARL PERFORM X in vacuum. Except for UV-Vis and XRF, others test uses HMSC–NiCoP-2.68 wt% sample.

4. Results and discussion

4.1 Morphology

Fig. 1(a), (b), (f) and (g) are the SEM images of HMSC–NiP and HMSC–NiCoP-2.68 wt% by the seed induced direct assembly fabrication, form which it can be clearly seen that the alloy nanoparticles is successfully loaded onto the surface of AHGMs. The yellow arrows in the figures point out the AHGMs silicate support and nickel-based alloy NPs. And the as-prepared surficial alloy single particles have a mean diameter of 46 ± 6 nm and 45 ± 8 nm in sample HMSC–NiP and HMSC–NiCoP-2.68 wt%, respectively, as is shown in Fig. S1.† Fig. 1(c–e) and (h–j) are the TEM and SADE images of HMSC–NiP and HMSC–NiCoP-2.68 wt%. From these images, it can also be found that the NiCoP and NiP alloy nanospheres dispersed separately on the surface of AHGMs, and they are almost polycrystalline which is beneficial to catalytic property (the red circles point out the different crystal regions). It is reported that the low degree of crystallization of materials may lead to the more crystal face defects and catalytically active sites.[1,29] This phenomenon echoes the catalytic property of the synthesized materials which is mentioned later. Different from those of the HMSC–NiP and HMSC–NiCoP-2.68 wt%, the surface topography of HMSC–Ni is much coarser (Fig. S2(b)†), which may be attributed to the low electrochemical reduction potential and thus the easy reduction nickle ions. On the other hand, it is found that the introducing of phosphorus is beneficial to the morphology control of nickel-based alloy nanoparticles. The optical microscopy images of various samples are shown in Fig. S3.† It can be seen obviously that the HGMs (Fig. S3(a)†) and AHGMs (Fig. S3(b)†) are transparent and glossy, while the synthesized HMSC–NiCoP-2.68 wt% (Fig. S3(c)†) is lightly transparent, indicating the successful assembly of nontransparent alloy particles on the AHGMs.

4.2 Elemental composition

To prove the successful synthesis of HMSC–NiCoP-2.68 wt%, their elemental composition is analyzed by powder XRD and EDX. In Fig. 2, a broad diffraction peak can be seen at 2θ of *ca.* 23°,which can indexed to amorphous silica from HGMs. After the deposition of alloy nanoparticles, several weak peaks of Ni (JCPDS #04-0850), Ni_2P (JCPDS #74-1385), Co (JCPDS #15-0806) appear at 44.4°, 44.6°, 44.9°, and 47.6°on the XRD pattern of the HMSC–NiCoP-2.68 wt%, while there are no obvious additional peaks in the case of HMSC–Ni and HMSC–NiP. The weak XRD peaks can be ascribed to two mains reasons: (I) compared to the support, the content of nanoparticles is extremely few (see the XRF results showing the content in Table S2†); (II) the small size and low crystallinity of the alloy nanoparticles. This is consistent with the results of HRTEM (Fig. 1). Whereas it can be obviously observed in the curve of pure NiCoP, the diffraction peak is actually obvious owing to its micron size and no support as seen in Fig. S4.† In order to further analyze the elemental composition of the target product, the EDX element mapping analysis of HMSC–Ni, HMSC–NiP, HMSC–NiCoP-2.68 wt% were carried out (Fig. S5†). From the element mapping patterns, it can be seen clearly that the Ni, Co, and P elements distribute uniformly on the surface of the support spheres.

4.3 Probable growth process of alloy NPs

In order to understand the formation process of alloy NPs, the morphology evolution of the NPs on the surface of the HGMs has been investigated by scanning electron microscopy (SEM) at various stages of the reaction. The SEM images of the samples obtained at various reaction stages and the proposed "directed assembly" formation process of the HMSC are shown in Fig. 3. On the one hand, during the activation process, palladium seeds are formed on the surface of the HGMs by amination-complexation-reduction steps (Fig. 3(b)). On the other hand, the reaction system is well designed to ensure the spontaneous reduction of metallic ions thermodynamiclly impossible. At the beginning of the reduction and deposition of alloy NPs, the palladium seeds serve as the active centres to ensure the *in situ* reduction and growth of the NPs on the surface of the HGMs (Fig. 3(c)). Afterwards, the directed deposition and growth of the alloy continues through self-catalyzed reduction, and a raspberry-like composite catalysts structure is obtained (Fig. 3(d)). Finally, along with the prolonged reaction time, the alloy NPs grows further and a dense NiCoP shell is formed (Fig. 3(e)). According to the above formation process, our directed assembly strategy holds several advantages. First, the size of the alloy nanoparticles can be adjusted by the reaction time. Secondly, the loading amount of the alloy nanoparticles can be tailored by adjusting the feeding amount of ionic solution. Third, our seeds induced direct assembly approaches can also be applied to the directed formation of other metallic NPs on various supports. For instances, we have successfully achieved the directed assembly of NiFeP NPs on AHGMs, and the nickel-

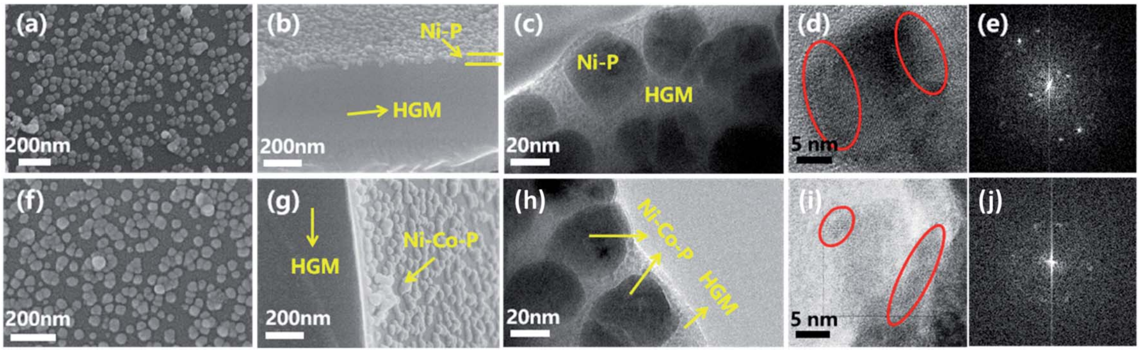

Fig. 1 SEM images of (a–e) HMSC–NiP, (f–j) HMSC–NiCoP-2.8 wt%. And (a), (d) are the surficial NPs of HMSC–NiP and HMSC–NiCoP-2.8 wt%; (b and g) are the cross section, respectively; (c and h) are the TEM images; (d and i) are the HETEM images; (e and j) are the electron selected diffraction patterns.

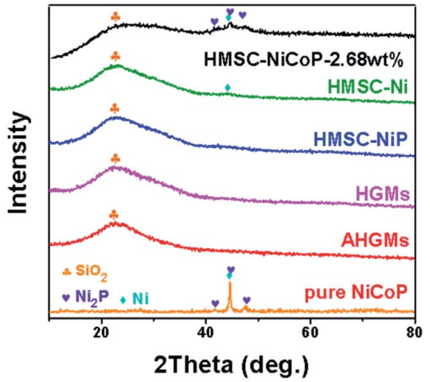

Fig. 2 XRD patterns of the HGMs, AHGMs, HMSC–Ni, HMSC–NiP, HMSC–NiCoP-2.68 wt% and pure NiCoP particles (obtained in the absence of HGMs).

based NPs on hollow phenolic resin microspheres (HPRM–NiCoP) Fig. S6.†

4.4 Catalytic property

It is well known that the reduction of aromatic nitro compounds to aromatic amines is a very important process in synthetic organic chemistry and production of many industrially important chemicals. Thus, we take the catalytic hydrogenation experiment of 4-NP at room temperature to assess the catalytic properties of AHGMs supported nickel-based alloy catalysts. The concentration of 4-NP in reduction process is monitored by UV-vis absorption spectroscopy (Fig. S7(a)†). After added $NaBH_4$, the 4-NP is evidenced by an absorption peak at 400 nm, while its reduzate 4-AP at 297 nm. The reduction reaction did not proceed in the absence of catalytic particles, since the reduction potential of 4-NP converted to 4-AP is 0.76 V, while that of borate-borohydride (H_3BO_3/BH_4^-) is −1.33 V. However, the reduction reaction commences when the AHGMs supported nickel-based alloy catalyst is added into the solution. The absorption of 4-NP at 400 nm decreases quickly while the absorption of 4-AP at 297 nm appears accordingly (Fig. S7(b)†). There is a linear relationship between $-\ln(C_t/C_0)$ (C_t refers to the concentration of 4-NP at time t and C_0 is the original concentration) and reaction time (t) in the reduction reaction catalyzed by AHGMs supported nickel-based alloy catalysts, suggesting that the reaction follows the first-order kinetics as shown in Fig. 4(a) and (b). Since the rate constant k is influenced by the amounts of the catalyst used, two kinds of the reaction rate constant are used to compare the catalytic property, the apparent rate constant k_A and the normalization rate constant k_N (the apparent rate constant k_A per the total weight of the alloy NPs except AHGMs). The loading amount (wt%) of the alloy is analyzed by XRF shown in Table S2.† The specific values of rate constants k_A and k_N are shown in Table 1.

The k_N of HMSC–Ni, HMSC–NiP, HMSC–NiCoP-2.68 wt% is 0.63 s^{-1} g^{-1}, 5.14 s^{-1} g^{-1}, 14.0 s^{-1} g^{-1}, respectively, which

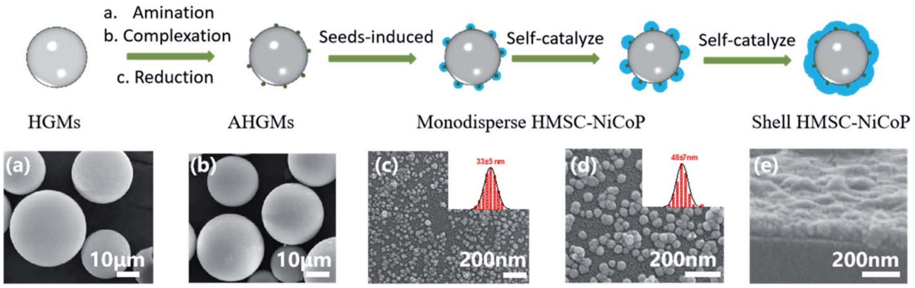

Fig. 3 The schematic illustration formation process of loading NiCoP NPs on HGMs through seeds induced direct assembly fabrication; (a–e) SEM images corresponding with the structural models above in scheme.

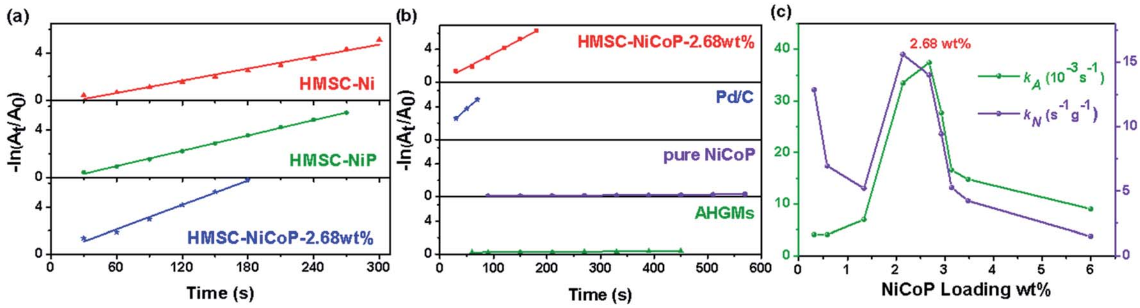

Fig. 4 The corresponding plot of $-\ln(C/C_0)$ *versus* reaction time t (a and b) and NiCoP loading amounts (c). (a) Silicate-nickel alloy composites doped with P and Co, (b) comparison among AHGMs, pure NiCoP, commercial 5 wt% Pd/C and synthesized HMSC–NiCoP-2.68 wt%, (c) the rate constant k_A and k_N as a function of NiCoP loading amounts in HMSC–NiCoP.

increases gradually. From these results, it is indicated that the doping of P and Co is beneficial to improve catalytic performance due to the synergistic effect of alloying. It is reported that alloying promotes the transfer of electrons, thereby promoting the catalytic reaction.[6] In comparison with the literature, our AHGMs supported nickel-based alloy catalysis exhibited better catalytic effect for 4-NP reduction reported (shown in Fig. S8†). Catalytic activity of HMSC–NiCoP-2.68 wt% is even better than some precious metal catalysts.

To investigate the loading amounts of effective active alloy NPs on catalytic hydrogenation performance, we prepare HMSC–NiCoP with different loading amounts (0.314 wt%–6.00 wt%), and named follow the same format as HMSC–NiCoP-2.68 wt%. We tuned the catalyst loading amounts through varying the mass ratio of mixed solution to AHGMs, and obtained the corresponding rate constants k_A and k_N curves of HMSC–NiCoP with different loading amounts. From the probable formation process of alloy NPs, it is found that when the loading amounts is small, the small NPs induced by the seeds are monodispersed on the surface of the AHGMs; with the increased loading amounts, the auto-catalytic reaction of the NPs continues until a dense shell is formed. The rate constant k_A and k_N as a function of loading amounts of HMSC–NiCoP curves is shown in Fig. 4(c). In the initial stage, the particles are small and sparse. Although the apparent rate of catalytic reaction is limited by the less loading amounts, the normalization rate is still high due to the small size effect of the surficial NPs. With the increased loading amounts, the proportion of effective catalyst NPs increases, and the apparent rate constant increases, accordingly. When the loading amount reaches 2.68 wt%, the optimized occupy of the loading sites on the HGMs is achieved. By this time, the surficial active sites of each single particle are sufficiently exposed with the formation of "raspberry" structure, and the catalytic reaction activity and the reaction rate are optimal. With the further increased loading amount, a dense layer composed of compactly stacked particles is formed, which inevitably leads to the inferior accessibility of the active sites, and thus much lower apparent and normalization rates. Therefore, the relative content of the carrier and the active material should be well balanced. When the loading amounts are small, the effective loading sites on the support cannot be fully utilized, and conversely, the active material does not work sufficiently. In the present work, we find that the maximum normalized reaction rate reaches 14.0 s^{-1} g^{-1} for the catalytic reduction of 4-NP when the loading amounts is 2.68 wt%.

Table 1 The kinetic results of different synthesized nickel-based catalysts

Sample	k_A (10^{-3} s^{-1})	k_N (s^{-1} g^{-1})	Conversion %
HMSC–Ni	17.0	0.63	99.4
HMSC–NiP	21.6	5.14	99.6
HMSC–NiCoP-2.68 wt%	37.4	14.0	99.8
AHGMs	0.444	3.31	31.7
Pure NiCoP	0.049	5.16×10^{-3}	27.5
Commercial Pd/C	58.2	11.64	99.3

To illustrate the necessity of support, nickel-based alloy composite catalysts without AHGMs supports were synthesized under the same reaction conditions as HMSC–NiCoP-2.68 wt%. The particle size is about 500 nm (which is ten times larger than AHGMs supported catalysts), and there is irreversible agglomeration (Fig. S4†). And the XRD results revealed the pure NiCoP has better crystallinity. Such a large size and high crystallinity results in lower catalytic efficiency (Fig. 4(b)). The k_N of pure NiCoP is 5.16×10^{-3} s^{-1} g^{-1}, which is three orders of magnitude smaller than that of HMSC–NiCoP-2.68 wt%. Commercial 5 wt% Pd/C is also investigated in this probe reaction with the same experimental conditions of HMSC–NiCoP-2.68 wt%. The k_N of commercial 5 wt% Pd/C is 11.64 s^{-1} g^{-1}, which is little higher than the as-obtained HMSC–NiCoP-2.68 wt%. The k_N of our obtained HMSC–NiCoP-2.68 wt% is much higher than some reported supported metal catalysts (Fig. S8†). Therefore, our HMSC–NiCoP-2.68 wt% product may be a promising replacement of commercial supported noble metal catalysts with comparable activity. Moreover, the catalytic reduction activity of AHGMs is found to exhibit a k_N of 3.31 s^{-1} g^{-1}. This indicates that AHGMs contributes less to the catalytic action of HMSC–NiCoP. In summary, the excellent catalytic activity of HMSC–NiCoP-2.68 wt% attributes to the little size and alloying of multiple components. The presence of the AHGMs support can

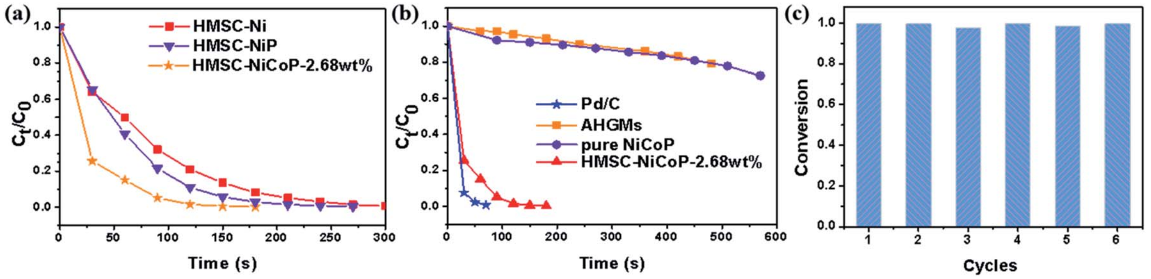

Fig. 5 (a) and (b) are the corresponding curves of 4-NP concentration *versus* reaction time with different catalysts; (c) the cycling runs in the catalytic reduction of 4-NP in the presence of the HMSC–NiCoP-2.68 wt% with $NaBH_4$.

regulate the growth and dispersion of the alloy particles, and favor the maintain and exert of the perfect catalytic performance of NPs.

The time-dependent C_t/C_0 curves are shown in Fig. 5. C_t/C_0 is directly given by the relative intensity of the respective absorbance A_t/A_0 of 4-NP according to the Beer–Lambert Law. It can be seen from Fig. 5(a) that within two minutes, the doping of P slightly accelerates the decrease of 4-NP concentration, and after the further doping of Co, the concentration of 4-NP decreases more rapidly. This indicates that the doping of P and Co is beneficial to the improvement of catalytic performance. As can be seen in Fig. 5(b), the HMSC–NiCoP-2.68 wt% has the same rapidly downward trend with commercial 5 wt% Pd/C. However, in the case of the AHGMs and pure NiCoP, the decreasing of C_t/C_0 is much slower. In addition, we also investigated the recyclability of the HMSC–NiCoP-2.68 wt% catalyst in 4-NP reduction. It is found that a conversion rate of above 97% can still be achieved after 6 cycles of reaction (Fig. 5(c)).

4.5 XPS analysis

To investigate the surface composition and chemical states and illustrate the electronic transfer of HMSC–Ni, HMSC–NiP and HMSC–NiCoP-2.68 wt% catalysts, the XPS analysis of our HMSC samples were carried out. The chemical states of Ni are investigated by analyzing the Ni 2p spectra. The spectra of Ni 2p could be resolved into six peaks corresponding to the $2p_{1/2}$ and $2p_{3/2}$ spin–orbit coupling, of which six peaks labeled as ν_1, ν_2, μ_1, μ_2, λ_1, and λ_2, assigning to Ni^0 and Ni^{2+}. For the Ni^0, the peaks are named as ν_1, ν_2, and the peaks of Ni^{2+} are denoted as μ_1, μ_2, the λ_1, λ_2 present satellite peaks. The exact position and peak area for each assigned peak are listed in Tables S3–S5.† Fig. 4 (a–c) show the XPS spectra of Ni 2p in sample HMSC–Ni, HMSC–NiP and HMSC–NiCoP, respectively. From the XPS analysis, Ni $2p_{3/2}$, Co $2p_{3/2}$ in HMSC–NiP and HMSC–NiCoP-2.68 wt% are positively shifted and $P_{3/2}$ is negatively shifted relative to the binding energy (BE) of metallic Ni(852.3 eV), Co(777.9 eV) and P (130.2 eV), implying a transfer of electron density from Ni and Co to P.[30] The same trend was also mentioned by Chun-Chao Hou.[6] With the doping of Co, both the BE of Ni and Co shifted toward higher energy, demonstrating a change of the Ni and Co electron density in Fig. 6(c and f). Furthermore, with the presence of Co, the shift value of Ni to high BE $(\mu''_1 \rightarrow \mu'_1)$ is much larger than that after only P-doping $(\mu'_1 \rightarrow \mu_1)$. Simultaneously, with the doping of Co, the

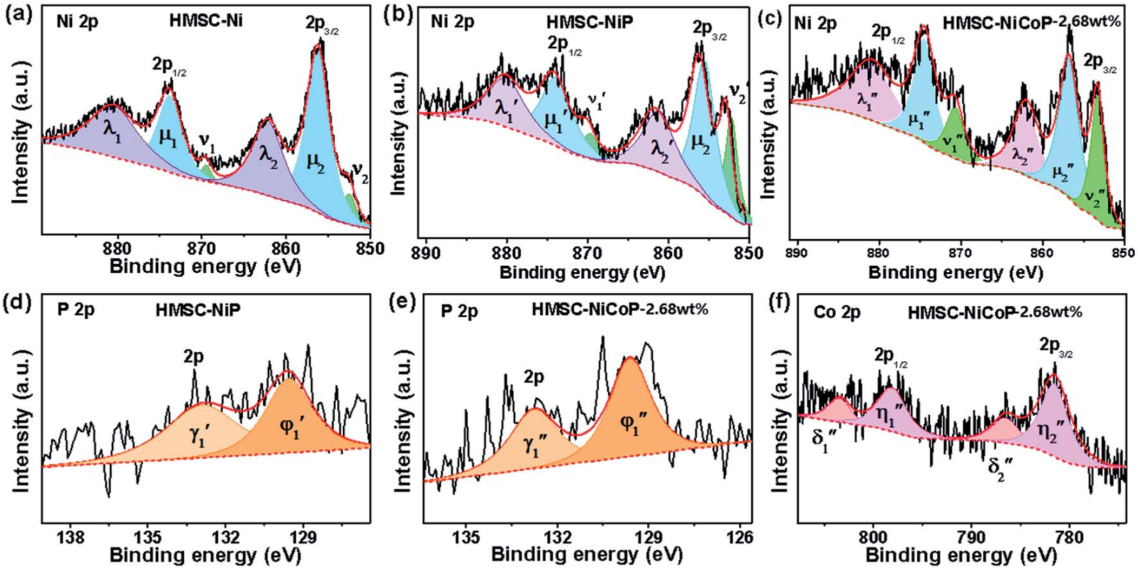

Fig. 6 X-ray photoelectron spectroscopy (XPS) spectrums of (a–c) Ni 2p, (d) and (e) P 2p, (f) Co 2p of HMSC–Ni, HMSC–NiP and HMSC–NiCoP-2.68 wt%, respectively, and all curves fitting is performed based on a Shirley-type background.

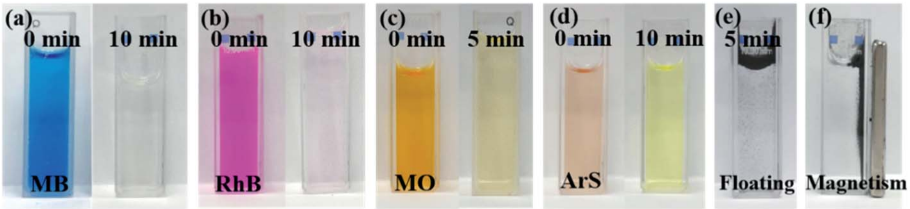

Fig. 7 Photographs of the decolorization of (a) MB, (b) RhB, (c) MO, (d) ArS catalyzed by the HMSC–NiCoP-2.68 wt%; (e) the HMSC–NiCoP-2.68 wt% catalyst floating on the aqueous solution; (f) the separation of HMSC–NiCoP-2.68 wt% catalyst by an magnet.

peak area of $P^{\delta-}$ in sample HMSC–NiCoP ($A_{\phi 1''}$) increases than the peak area in HMSC–NiP ($A_{\phi 1'}$), which means that the more electrons are transferred from the metal to the P center after Co doping. Based on the above discussions, it is convinced that electrons transfer from metal to P centers occurred, which is beneficial for catalytic hydrogenation reaction.[31]

4.6 Catalytic diversity and recycling

Printing and dyeing wastewater usually contains many organic colored dyes, such as MB, RhB, MO, and ArS. It is also of great importance to decolorize colored wastewaters containing these contaminates in the wastewater treatment industry. Herein, the decolorization reduction reaction of MB, RhB, MO, ArS catalyzed by the HMSC–NiCoP-2.68 wt% is also investigated. These dyes emerge different degrees of decoloration with different time as shown in Fig. 7. The MB, RhB and ArS become nearly colorless after 10 minutes and the change of absorbance is shown in Fig. S11.† Besides, the obtained HMSC–NiCoP-2.68 wt% catalyst can float by its ultralow density originated form their hollow interior (Fig. 7(e)). In addition to floating separation, our synthetic HMSC–NiCoP-2.68 wt% catalysts also exhibit a ferromagnetic nature with a saturated magnetization of 1.49 emu g^{-1} (Fig. S12†). This opens an additional avenue to achieve high efficient separation assisted by an external magnetic field (Fig. 7(f)).

5. Conclusion

In summary, we have successfully developed a reliable and versatile strategy for the large scale synthesis of low density magnetic HGMs supported nickel-based alloy composites as excellent catalysts for catalytic hydrogenation of 4-NP. Benefitting from the synergistic effect among heterogeneous elements electron transfer process, sufficient utilization of the loading sites on the HGMs and high dispersion, the HMSC–NiCoP-2.68 wt% shows boosted normalized rate constant at ambient temperature, which is comparable to some supported precious metal catalysts. Also a high retention ratio 97% of the catalytic activity is achieved after 6 cycles of application. These findings not only enrich the candidates of noble-metal-free catalysts and provide a new type of catalysts combining floating separation and magnetic separation, but also open an additional avenue to achieve controllable alloying of metallic catalysts. This synthetic strategy holds strong potential to be extended to the preparation and property control of other metal nanocatalysts on various supports.

Conflicts of interest

The authors declare no competing financial interest.

Acknowledgements

This work was supported by the National Key R&D Program of China (projects No. 2016YFC0304505 & 2019YFC0311401), the Strategic Priority Research Program of Chinese Academy of Science (XDA22010202) and the National Natural Science Foundation of China (projects No. 51872298).

References

1 L. Xu, H. W. Liang, Y. Yang and S. H. Yu, Stability and Reactivity: Positive and Negative Aspects for Nanoparticle Processing, *Chem. Rev.*, 2018, **118**(7), 3209–3250.

2 J. Zheng, Y. Dong, W. Wang, Y. Ma, J. Hu, X. Chen and X. Chen, In situ loading of gold nanoparticles on Fe3O4@SiO2 magnetic nanocomposites and their high catalytic activity, *Nanoscale*, 2013, **5**(11), 4894.

3 M. Raula, M. H. Rashid, S. Lai, M. Roy and T. K. Mandal, Solvent-adoptable polymer Ni/NiCo alloy nanochains: highly active and versatile catalysts for various organic reactions in both aqueous and nonaqueous media, *ACS Appl. Mater. Interfaces*, 2012, **4**(2), 878–889.

4 M. H. Rashid, M. Raula and T. K. Mandal, Polymer assisted synthesis of chain-like cobalt-nickel alloy nanostructures: Magnetically recoverable and reusable catalysts with high activities, *J. Mater. Chem.*, 2011, **21**(13), 4904.

5 X. Zhang, Y. Zhao, X. Jia, Y. Zhao, L. Shang, Q. Wang, G. I. N. Waterhouse, L.-Z. Wu, C.-H. Tung and T. Zhang, Silica-Protected Ultrathin Ni3 FeN Nanocatalyst for the Efficient Hydrolytic Dehydrogenation of NH3 BH3, *Adv. Energy Mater.*, 2018, **8**(12), 1702780.

6 C.-C. Hou, Q. Li, C.-J. Wang, C.-Y. Peng, Q.-Q. Chen, H.-F. Ye, W.-F. Fu, C.-M. Che, N. López and Y. Chen, Ternary Ni–Co–P nanoparticles as noble-metal-free catalysts to boost the hydrolytic dehydrogenation of ammonia-borane, *Energy Environ. Sci.*, 2017, **10**(8), 1770–1776.

7 X. Du, C. Zhao, X. Li, H. Huang, Y. Wen, X. Zhang and J. Li, Novel yolk-shell polymer/carbon@Au nanocomposites by

using dendrimer-like mesoporous silica nanoparticles as hard template, *J. Alloys Compd.*, 2017, **700**, 83–91.

8 D. Formenti, F. Ferretti, F. K. Scharnagl and M. Beller, Reduction of Nitro Compounds Using 3d-Non-Noble Metal Catalysts, *Chem. Rev.*, 2019, **119**(4), 2611–2680.

9 J. Song, Z.-F. Huang, L. Pan, K. Li, X. Zhang, L. Wang and J.-J. Zou, Review on selective hydrogenation of nitroarene by catalytic, photocatalytic and electrocatalytic reactions, *Appl. Catal. B Environ.*, 2018, **227**, 386–408.

10 J. Deng, P. Ren, D. Deng and X. Bao, Enhanced electron penetration through an ultrathin graphene layer for highly efficient catalysis of the hydrogen evolution reaction, *Angew. Chem. Int. Ed.*, 2015, **54**(7), 2100–2104.

11 K. Hu, T. Ohto, L. Chen, J. Han, M. Wakisaka, Y. Nagata, J.-i. Fujita and Y. Ito, Graphene Layer Encapsulation of Non-Noble Metal Nanoparticles as Acid-Stable Hydrogen Evolution Catalysts, *ACS Energy Lett.*, 2018, **3**(7), 1539–1544.

12 M. Ledendecker, J. S. Mondschein, O. Kasian, S. Geiger, D. Gohl, M. Schalenbach, A. Zeradjanin, S. Cherevko, R. E. Schaak and K. Mayrhofer, Stability and Activity of Non-Noble-Metal-Based Catalysts Toward the Hydrogen Evolution Reaction, *Angew. Chem. Int. Ed.*, 2017, **56**(33), 9767–9771.

13 Z. Li, L. Mo, Y. Kathiraser and S. Kawi, Yolk–Satellite–Shell Structured Ni–Yolk@Ni@SiO2 Nanocomposite: Superb Catalyst toward Methane CO2 Reforming Reaction, *ACS Catal.*, 2014, **4**(5), 1526–1536.

14 J. Bian, F. Lan, Y. Wang, K. Ren, S. Zhao, W. Li, Z. Chen, J. Li and J. Guan, Facile morphology-controlled synthesis of nickel-coated graphite core-shell particles for excellent conducting performance of polymer-matrix composites and enhanced catalytic reduction of 4-nitrophenol, *Nanotechnology*, 2018, **29**(14), 145602.

15 J. Cai, J. Huang, S. Wang, J. Iocozzia, Z. Sun, J. Sun, Y. Yang, Y. Lai and Z. Lin, Crafting Mussel-Inspired Metal Nanoparticle-Decorated Ultrathin Graphitic Carbon Nitride for the Degradation of Chemical Pollutants and Production of Chemical Resources, *Adv. Mater.*, 2019, **31**(15), e1806314.

16 R. Krishna, D. M. Fernandes, J. Ventura, C. Freire and E. Titus, Novel synthesis of highly catalytic active Cu@Ni/RGO nanocomposite for efficient hydrogenation of 4-nitrophenol organic pollutant, *Int. J. Hydrogen Energy*, 2016, **41**(27), 11608–11615.

17 G.-M. Shi, S.-T. Li, F.-N. Shi, X.-F. Shi, S.-H. Lv and X.-B. Cheng, A facile strategy for synthesis of Ni@C(N) nanocapsules with enhanced catalytic activity for 4-nitrophenol reduction, *Colloid. Surface. Physicochem. Eng. Aspect.*, 2018, **555**, 170–179.

18 Y. Zhou, Y. Zhu, X. Yang, J. Huang, W. Chen, X. Lv, C. Li and C. Li, Au decorated Fe3O4@TiO2 magnetic composites with visible light-assisted enhanced catalytic reduction of 4-nitrophenol, *RSC Adv.*, 2015, **5**(62), 50454–50461.

19 X. J. Yang, C. Y. Wang, R. Y. Gao, Z. M. Lu, X. H. Zhang, X. F. Yu and L. L. Li, Non-noble metallic nanoparticles supported on titania spheres as catalysts for hydrogen generation from hydrolysis of ammonia borane under ultraviolet light irradiation, *Int. J. Hydrogen Energy*, 2018, **43**(34), 16556–16565.

20 Y. Chen, Y. Zhang, Q. Kou, Y. Liu, D. Han, D. Wang, Y. Sun, Y. Zhang, Y. Wang, Z. Lu, L. Chen, J. Yang and S. G. Xing, Enhanced Catalytic Reduction of 4-Nitrophenol Driven by Fe(3)O(4)-Au Magnetic Nanocomposite Interface Engineering: From Facile Preparation to Recyclable Application, *Nanomaterials*, 2018, **8**(5), 353.

21 V. B. Cashin, D. S. Eldridge, A. Yu and D. Zhao, Surface functionalization and manipulation of mesoporous silica adsorbents for improved removal of pollutants: a review, *Environ. Sci.: Water Res. Technol.*, 2018, **4**(2), 110–128.

22 W. Gac, W. Zawadzki, G. Słowik, A. Sienkiewicz and A. Kierys, Nickel catalysts supported on silica microspheres for CO2 methanation, *Microporous Mesoporous Mater.*, 2018, **272**, 79–91.

23 J. Dai, H. Zou, R. Wang, Y. Wang, Z. Shi and S. Qiu, Yolk–shell Fe3O4@SiO2@PMO: amphiphilic magnetic nanocomposites as an adsorbent and a catalyst with high efficiency and recyclability, *Green Chem.*, 2017, **19**(5), 1336–1344.

24 J. Liu, S. Z. Qiao, Q. H. Hu and G. Q. Lu, Magnetic nanocomposites with mesoporous structures: synthesis and applications, *Small*, 2011, **7**(4), 425–443.

25 Z. Xiong, H. Zhang, W. Zhang, B. Lai and G. Yao, Removal of nitrophenols and their derivatives by chemical redox: A review, *Chem. Eng. J.*, 2019, **359**, 13–31.

26 P. Zhao, X. Feng, D. Huang, G. Yang and D. Astruc, Basic concepts and recent advances in nitrophenol reduction by gold- and other transition metal nanoparticles, *Coord. Chem. Rev.*, 2015, **287**, 114–136.

27 Z. An, S. Pan, J. Zhang and G. Song, Facile synthesis of urchin-like glass/nickel core/shell composite hollow spheres, *Dalton Trans.*, 2008, (38), 5155–5158.

28 P. Wang, B. Liao, Z. An, K. Yan and J. Zhang, Measurement and calculation of cryogenic thermal conductivity of HGMs, *Int. J. Heat Mass Transfer*, 2019, **129**, 591–598.

29 V. Valtchev and L. Tosheva, Porous nanosized particles: preparation, properties, and applications, *Chem. Rev.*, 2013, **113**(8), 6734–6760.

30 H. Sun, X. Xu, Z. Yan, X. Chen, F. Cheng, P. S. Weiss and J. Chen, Porous Multishelled Ni2P Hollow Microspheres as an Active Electrocatalyst for Hydrogen and Oxygen Evolution, *Chem. Mater.*, 2017, **29**(19), 8539–8547.

31 S. Cao, Y. Chen, C. J. Wang, P. He and W. F. Fu, Highly efficient photocatalytic hydrogen evolution by nickel phosphide nanoparticles from aqueous solution, *Chem Commun*, 2014, **50**(72), 10427–10429.